KeAi
CHINESE ROOTS
GLOBAL IMPACT

Contents lists available at ScienceDirect

Petroleum Science

journal homepage: www.keaipublishing.com/en/journals/petroleum-science



Original Paper

Real-time NMR investigation of water infiltration mechanisms and pore structure evolution in fractured sandstone near-wellbore regions



Sheng-Feng Wu, Yong-Fa Zhang, Yu Zhao*, Chao-Lin Wang, Jing Bi, An-Fa Long, Yan Li

College of Civil Engineering, Guizhou University, Guiyang, 550025, Guizhou, China

ARTICLE INFO

Article history: Received 24 March 2025 Received in revised form 19 May 2025 Accepted 26 June 2025 Available online 7 July 2025

Edited by Meng-Jiao Zhou

Keywords: Water infiltration Pore evolution Near-wellbore damage RT-NMR Sandstone

ABSTRACT

During the exploitation of sandstone gas reservoirs, natural fractures near the wellbore affect water infiltration and pore evolution; however, the impact mechanisms of these fractures remain unclear. This study utilized real-time nuclear magnetic resonance (RT-NMR) technology to investigate the influence of near-wellbore fracture angle (α) at 0°, 15°, 30°, and 45° on water infiltration, migration patterns, and pore evolution mechanisms during water injection. Throughout the experiments, T2 curves and magnetic resonance imaging (MRI) were monitored in real time during the water injection process. The pore evolution and water infiltration were translated by the evolution of T_2 curves and MRI. The results show that increasing injection pressure (P_{inj}) transforms adsorption pores into seepage pores, leading to enhanced pore damage. Pore damage predominantly occurs during the rapid pressurization stage and is concentrated around the near-wellbore fracture. The maximum infiltration area and rate were observed at $\alpha=0^{\circ}$, while the minimum values occurred at $\alpha=45^{\circ}$, which can be attributed to the significant influence of α on water infiltration and migration pathways. The increasing inclination of the infiltration front with α is attributed to the fact that the rate of water infiltration along the fracture wall is always higher than that at the fracture tip. In field fracturing, it is recommended to adjust the perforation direction to align with the natural fracture orientation and optimize pressurization strategies by reducing the slow pressurization duration while extending the rapid pressurization stage. These findings can provide important guidance for setting fracturing sections and optimizing injection parameters in sandstone gas reservoir exploitation.

© 2025 The Authors. Publishing services by Elsevier B.V. on behalf of KeAi Communications Co. Ltd. This is an open access article under the CC BY-NC-ND license (http://creativecommons.org/licenses/by-nc-nd/4.0/).

1. Introduction

As a supplement to conventional energy, tight sandstone gas is considered a relatively environmentally friendly unconventional energy source. However, the low permeability, complex geology, natural fracture development, and great burial depth of tight sandstone gas reservoirs pose significant development challenges (Jia et al., 2022). Hydraulic fracturing technology is an effective means of extracting unconventional oil and gas resources (Zhang et al., 2023; Zhao et al., 2024a), and it has been widely applied in the exploitation of sandstone gas (Li et al., 2019; Stanchits et al.,

E-mail address: zhaoyucivil@126.com (Y. Zhao).

Peer review under the responsibility of China University of Petroleum (Beijing).

2014). Hydraulic fracturing technology involves injecting fracturing fluid into the reservoir using high-pressure pumps. When the injection pressure exceeds the breakdown pressure of the reservoir, hydraulic fractures are created (Jiang et al., 2019; Yan et al., 2021). The continuous injection of fracturing fluid facilitates the progressive propagation of hydraulic fractures, which subsequently interconnect with natural fractures within the reservoir. This interaction leads to an extensive and complex fracture network, thereby significantly enhancing reservoir permeability and optimizing gas extraction efficiency from tight sandstone formations.

Randomly distributed natural fractures are naturally developed in sandstone reservoirs due to geological formations and crustal movements (Abe et al., 2021). Natural fractures affect the initiation and propagation of hydraulic fractures (Liu et al., 2022). Researchers have conducted extensive research on the impact of

 $[\]ast$ Corresponding author.

natural fractures on hydraulic fracturing (Xu et al., 2019; Zhao et al., 2019b). As demonstrated by Zeng and Liu (2010), the propagation and morphology of hydraulic fractures in tight sandstone reservoirs are significantly influenced and structurally constrained by natural fracture networks. This finding has been corroborated by Liu et al. (2014) through laboratory experiments, further validating the critical role of natural fractures in hydraulic fracture propagation, Lamont and Jessen (1963) investigated the influence of the angle between the hydraulic fracture and the natural fracture on the behavior of the hydraulic fracture. They observed that when this angle is small, ranging from 30° to 60°, the hydraulic fracture directly penetrates the natural fracture, resulting in a deviation or steering of the hydraulic fracture's path. Published research has centered on elucidating the influence of natural fractures on the propagation behavior of hydraulic fractures, as well as examining the intersection between hydraulic and natural fractures (Fu et al., 2024). In the context of sandstone gas extraction utilizing hydraulic fracturing technology, the presence of natural fractures within the fracturing section is an inevitable geological factor (as illustrated in Fig. 1). Near-wellbore natural fractures significantly govern fracturing fluid flow. However, systematic studies on their impacts remain lacking, particularly regarding how near-wellbore natural fracture orientations affect fluid infiltration and migration patterns during hydraulic fracturing.

Compared to other reservoirs (e.g., shale and granite), sandstone reservoirs typically contain higher clay mineral content and exhibit more developed pore spaces, where significant water infiltration occurs (Chitrala et al., 2013; Jia et al., 2021), During hydraulic fracturing zones, significant fluid infiltration is observed at the fracturing section due to the continuous injection of fracturing fluid. The fracturing fluid infiltration induces substantial penetration into the rock matrix, leading to significant modifications in lithological characteristics and stress distribution within the affected formation zone (Fazio et al., 2023). Some research indicates that water infiltration can influence the failure properties of sandstone, and reduce the breakdown pressure of the reservoir (Li et al., 2023b; Wang et al., 2021). Fluid infiltration significantly influences hydraulic fracturing behavior, as demonstrated by Zhuang et al.'s (2019) hydraulic fracturing studies with varying injection rates. Li et al. (2023a) found that fluid infiltration

significantly reduces the microseismicity during the initiation and propagation of hydraulic fractures in tight sandstone reservoirs. Fazio et al. (2021) conducted hydraulic fracturing studies using two sandstones with different porosities, and they noted that high-permeability sandstones inhibit hydraulic fracture generation, while matrix permeability controls fracture propagation. Chitrala et al.'s (2013) research results demonstrate that water infiltration occurs along the propagation path of hydraulic fractures. Bandara et al.'s (2022) study shows that as the porosity of the rock increases, the fluid permeability also increases, leading to a more complex and tortuous fracture network. Fluid infiltration significantly impacts hydraulic fracture initiation and propagation during hydraulic fracturing. As shown in triaxial compression experiments conducted by Li et al. (2023a) on sandstones with different infiltration volumes, rock-damage cracks consistently appear around the dry-wet boundary, which is the result of fluid infiltration. Consequently, investigating fluid infiltration behavior during water injection is crucial. Understanding pore damage mechanisms, especially natural fractures near fracturing zones, significantly informs hydraulic fracturing design.

During the hydraulic fracturing injection process, the damage evolution near the wellbore directly affects the hydraulic fracture initiation and propagation state (Chang et al., 2022). Commonly used non-destructive monitoring of damage (fractures) includes optical direct observation, X-ray CT scanning, acoustic emission monitoring, and ultrasonic velocity monitoring (Liu et al., 2018; Zhang et al., 2024; Zhou et al., 2018). These methods fail to capture real-time fracturing dynamics, particularly pore damage nucleation and coalescence in near-wellbore zones during fluid injection. These conventional methods do not provide a better way to monitor the damage on the rock pore scale due to water injection. Hence, some researchers have turned to NMR techniques to study the evolution of sandstone pore structures before and after conducting experiments (Geng et al., 2023). Compared to conventional methods, the NMR technique can characterize microscale pore distribution (Lu et al., 2020). Ma et al. (2021) evaluated the impact of water and liquid CO₂ induced fracturing utilizing NMR technology and discovered that liquid CO₂ possesses greater potential for microfracture generation within sandstone reservoirs. On the other hand, Wang et al. (2022a) analyzed the changes in microporosity of specimens before and after testing

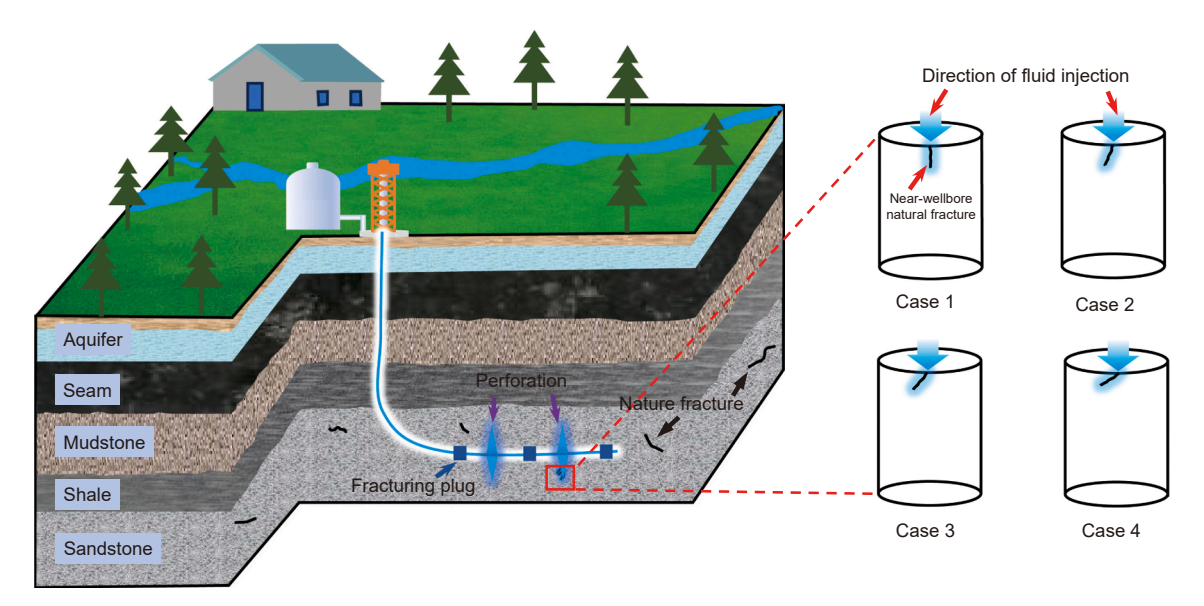


Fig. 1. Diagram of permeability enhancement technology for sandstone reservoirs.

based on the changes in the T_2 curve of laminated sandstones before and after fracturing. Wei et al. (2017) conducted low-field NMR analysis on specimens before and after hydraulic fracturing and concluded that micro-fractures were more developed after hydraulic fracturing based on the changes observed in the T_2 curve. These studies only focus on the changes before and after hydraulic fracturing, whereas hydraulic fracturing is a dynamic process. The dynamic evolution of pore damage, fluid infiltration around the wellbore, and fluid migration are crucial factors for initiating hydraulic fractures. Therefore, it is necessary to monitor, in real-time, fluid infiltration, fluid migration, and pore evolution within natural fractures in the near-wellbore region during hydraulic fracturing, utilizing NMR as a non-destructive monitoring technique. This study investigates the fluid infiltration and migration

characteristics of the near-wellbore natural fractures and the mechanism of pore damage accumulation and nucleation induced by fluid injection.

This study systematically investigated the impact of nearwellbore natural fractures, as illustrated in the four distinct cases presented in Fig. 1, on three critical aspects of water injection processes: water infiltration, water migration, and pore evolution mechanisms. To achieve these research objectives, a series of specimens with prefabricated fracture angles (α) of 0°, 15°, 30°, and 45° (Fig. 2(a)) were designed and experimented with using distilled water injection. The RT-NMR technology was employed to monitor changes in T_2 curves and MRI during the injection process. The study analyzes a comprehensive analysis of the evolution of $P_{\rm ini}$, water infiltration, migration patterns, and the distribution

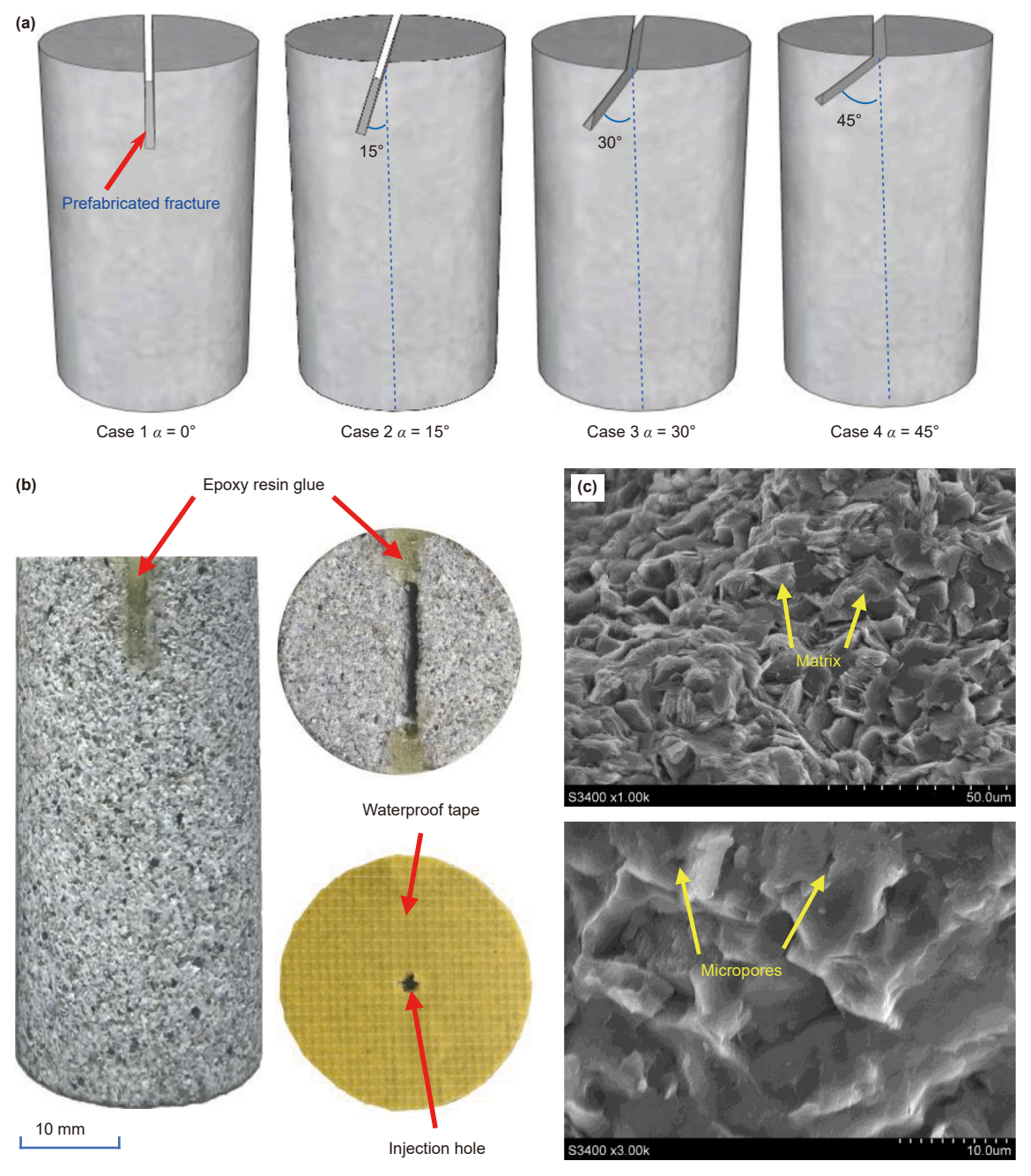


Fig. 2. Specimens of sandstone. (a) Specimen preparation 3D diagram. (b) The specimen with the epoxy resin glue and waterproof tape. (c) SEM of the sandstone specimen.

characteristics of pore structures in near-wellbore natural fractures with varying α . It explores the influence of α on water infiltration behavior, as well as the mechanisms underlying water infiltration and pore damage. Based on these findings, the research provides valuable insights for setting fracturing sections and optimizing injection parameters in the field-scale fracturing design of tight sandstone gas reservoirs.

2. Materials and methods

2.1. Specimen preparation

The sandstone specimens used in this study were taken from the Ordos Basin, Inner Mongolia, China. The sandstone blocks were machined into 25×50 mm cylindrical specimens. The average uniaxial compressive strength of the experimental specimen is 62.37 ± 3.85 MPa, the permeability was measured as $(50.29 \pm 4.77) \times 10^{-17}$ m². To simulate the influence of nearwellbore natural fractures on hydraulic fracturing processes, a 2 mm wide and 10 mm long prefabricated fracture was precisely engineered at the top surface of cylindrical rock specimens. A prefabricated angle, denoted as α , was defined as the angle between the prefabricated fracture and the axis of the specimen (see Fig. 2(a)). The axis direction of the specimen also corresponds to the water injection direction. The specimen number and some parameters are shown in Table 1.

To prevent water from leaking into the edge of the specimen from both ends of the prefabricated fracture and affecting the experiment results, the prefabricated fracture ends were sealed using epoxy resin glue (see Fig. 2(b)). In addition, to prevent the water from entering the specimen through any part other than the prefabricated fracture at the top during the water injection process, the waterproof tape was applied on the top of the specimen

(see Fig. 2(b)). An injection hole with a diameter of 2 mm was drilled to ensure water injection into the prefabricated fracture during the water injection process. Additionally, scanning electron microscope (SEM) images (see Fig. 2(c)) revealed the presence of micropores between the grains of the sandstone, highlighting the complex pore structure that may influence water behavior. This intricate network of micropores can facilitate enhanced water retention and distribution within the rock, potentially affecting the effectiveness of the hydraulic fracturing process (Zhang et al., 2025).

2.2. Experiment apparatus and procedure

The experiment equipment comprises three parts: I water injection system, II pressure loading system, and III NMR system (see Fig. 3(a)). The water injection system (I) comprises a computerized control system and two syringe pumps. The syringe pumps can inject water in either constant pressure mode or constant flow mode, providing a pressure range of 0.10–40 MPa and an injection rate range of 0.001-40 mL/min. The two pumps can automatically replenish the water and activate the alternate pump based on the remaining water levels under computerized control. This system ensures the seamless operation of the experiment by maintaining a steady supply of water, thereby preventing interruptions and supporting consistent experimental conditions throughout the process. The pressure loading system (II) was employed to apply controlled pressure to the specimen. In this investigation, Fluorinert FC-40, a hydrogen-free (1H) chemical compound, was utilized as the pressure medium for both axial and confining pressure applications. The selection of Fluorinert FC-40 was based on its unique property of being devoid of hydrogen nuclei, which ensures that it does not interfere with or compromise the accuracy of T_2 and MRI measurements during the experimental procedures. The

Table 1 Specimen parameters.

Specimen number	Fracture angle $lpha$, $^{\circ}$	P-wave velocity, km/s	Schematic diagram
#1	0	3.06 ± 0.01	F efshrioded flacture
#2	15	3.05 ± 0.02	15
#3	30	3.03 ± 0.02	357
#4	45	3.03 ± 0.02	20
#5	45	3.05 ± 0.02	43

Petroleum Science 22 (2025) 4195-4210

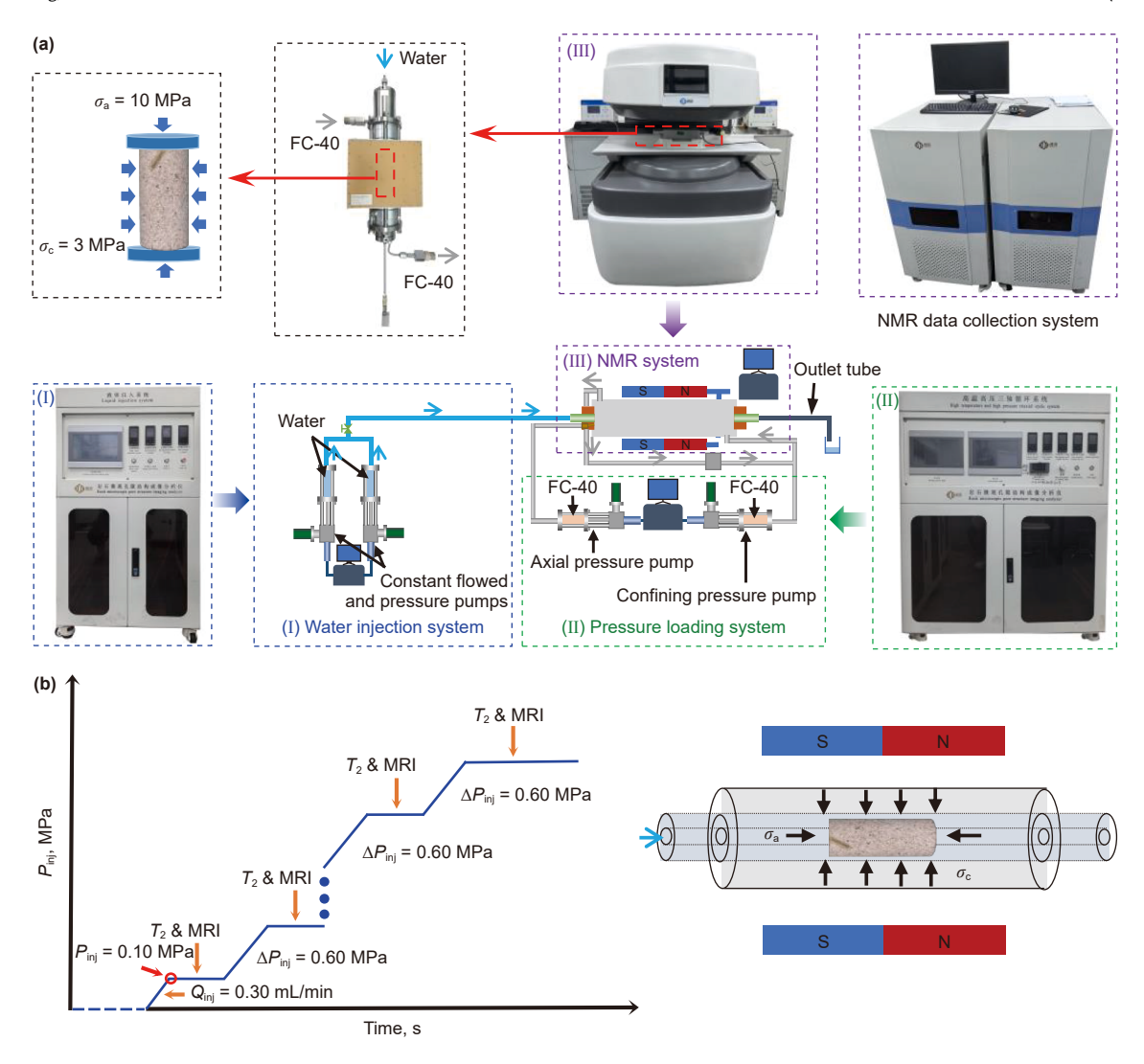


Fig. 3. Experimental equipment and process. (a) Experimental system and equipment diagram. (b) Schematic diagram of the experimental process.

pressure loading system (II) can apply a maximum of 100 MPa axial pressure and 40 MPa confining pressure to the experiment. The NMR system (III) MacroMR12-150H-I (Niumag Corporation, Suzhou, China) is used to characterize the pore and water infiltration. The NMR system (III) works under a magnetic field strength of 0.3 T, a resonance frequency of 12 MHz, and a temperature of 25–32 °C. The gradient magnetic fields have a maximum intensity of 0.15 T/m. In this study, T_2 curve and MRI sequences were obtained for pore and structure analysis. The test sequence for T_2 is CPMG, with an echo time of 0.30 ms and a waiting time of 2000 ms The MRI test sequence is HSE, with an echo time of 5.60 ms and a waiting time of 500 ms.

Before the injection of water, all specimens were subjected to a standardized drying process in a laboratory oven maintained at 105 °C for 24 h to ensure complete removal of pore water, thereby eliminating potential interference with experimental measurements (Jia et al., 2024). Next, the specimens were allowed to cool naturally to ambient temperature (25 \pm 2 °C) under controlled laboratory conditions before proceeding with the water injection experiments. The water injection experiment was performed under precisely controlled triaxial stress conditions, with a confining pressure of 3 MPa and an axial pressure of 10 MPa. A constant injection rate of 0.30 mL/min was maintained throughout the

experiment using a precision syringe pump to ensure consistent fluid delivery. The water injection protocol required systematic implementation of two critical steps: initial system activation for complete pipeline purging to ensure uniform water discharge and air removal, followed by proper specimen connection. This standardized approach effectively minimizes experimental errors caused by air entrapment in the injection system. Once the $P_{\rm inj}$ has reached 0.10 MPa, the initial T_2 and MRI tests were conducted. We performed interval measurements of T_2 and MRI signals at 0.60 MPa injection pressure increments, and recorded final measurements at peak injection pressure ($P_{\rm max}$). The specific experiment flow chart is shown in Fig. 3(b). It should be emphasized that the acquisition time for both T_2 and MRI tests was sufficiently short (typically less than 240 s), meaning that changes in the pore structure of the specimen were negligible during the tests.

2.3. Date processing

The pore distribution inside the specimen can be obtained depending on the T_2 relaxation time (Ge et al., 2019). The T_2 relaxation time can be calculated according to the following equation:

$$\frac{1}{T_2} \approx \rho_2 \left(\frac{S}{V}\right) = F_S \frac{\rho_2}{r} \tag{1}$$

where T_2 is the transverse relaxation time, ms; ρ_2 is the surface relaxation rate, nm/ms; S is the pore surface area, nm²; V is the fluid volume, nm³; r is the pore radius, nm; and F_S is a geometric factor. The cumulative volume fraction S_V of pores with a radius less than r can be expressed as (Zhang and Weller, 2014):

$$S_{V} = \frac{V(\langle r)}{V_{s}} = \frac{r^{3-D} - r_{\min}^{3-D}}{r_{\max}^{3-D} - r_{\min}^{3-D}}$$
 (2)

where D is the NMR fractal dimension. In general, r_{\min} is far less than r_{\max} . Hence, Eq. (2) can be simplified as:

$$S_{V} = \frac{V(\langle r)}{V_{s}} = \frac{r^{3-D}}{r_{\text{max}}^{3-D}} = \frac{T_{2}^{3-D}}{T_{2\text{max}}^{3-D}}$$
(3)

Taking the logarithm of both sides of Eq. (4) yields

$$ln(S_V) = (3 - D)ln(T_2) + (D - 3)ln(T_{2max})$$
(4)

In injection water experiments, fluid molecules (1 H) in the pores inside the specimen are magnetized under the action of an applied magnetic field and the NMR phenomenon occurs. The pore structure of the specimen can be categorized into adsorption pores (0.01–10 ms) and seepage pores (>10 ms) according to the magnitude of the relaxation time T_{2} (Geng et al., 2023; Li et al., 2020).

After applying axial and confining pressure to the specimen and allowing it to stabilize, the MRI scan of the specimen was subsequently performed. The resulting images were analyzed, and it was determined that the average grayscale value of the specimen was below 380. Note that no water has been injected into the

specimen at this time. Therefore, to reduce the impact of noise on the observation of experimental results, the minimum intensity threshold for MRI was set at 380. To more precisely quantify the impact of varying α on water infiltration, the cumulative gray values counted excluded the corresponding gray values of the prefabricated fractures themselves. Before $P_{\rm inj}$ rises to 0.10 MPa, the water injected into the specimen primarily fills the prefabricated fracture space, with almost no water penetrating into the rock pores. To better quantify the water infiltration during the water injection process, we ignore the infiltration amount before $P_{\rm inj}$ reaches 0.10 MPa and take the cumulative T_2 signal at $P_{\rm ini} = 0.10$ MPa as the signal amount representing the water in the prefabricated fracture. The difference between the cumulative T_2 signal in each stage of the water injection process and the baseline T_2 signal measured at $P_{\text{ini}} = 0.10$ MPa can be used as an indicator of water infiltration into the specimen during that stage. It should be emphasized that all data processing methods employed do not alter the experimental results; they are solely used to emphasize the patterns of water infiltration and pore evolution.

3. Results and analysis

3.1. Evolution of injection pressure

Fig. 4 shows a statistical plot of the variation of $P_{\rm inj}$, axial pressure ($\sigma_{\rm a}$), and confining pressure ($\sigma_{\rm c}$) with injection time. It is worth noting that we only considered the process of water pressurization, ignoring the testing stages of T_2 and MRI. Overall, regardless of the α , we can categorize the injection water process into four typical stages: slow pressurization stage (I), stabilized pressurization stage (II), rapid pressurization stage (III), and constant pressure stage (IV). The water pressurization curve exhibited

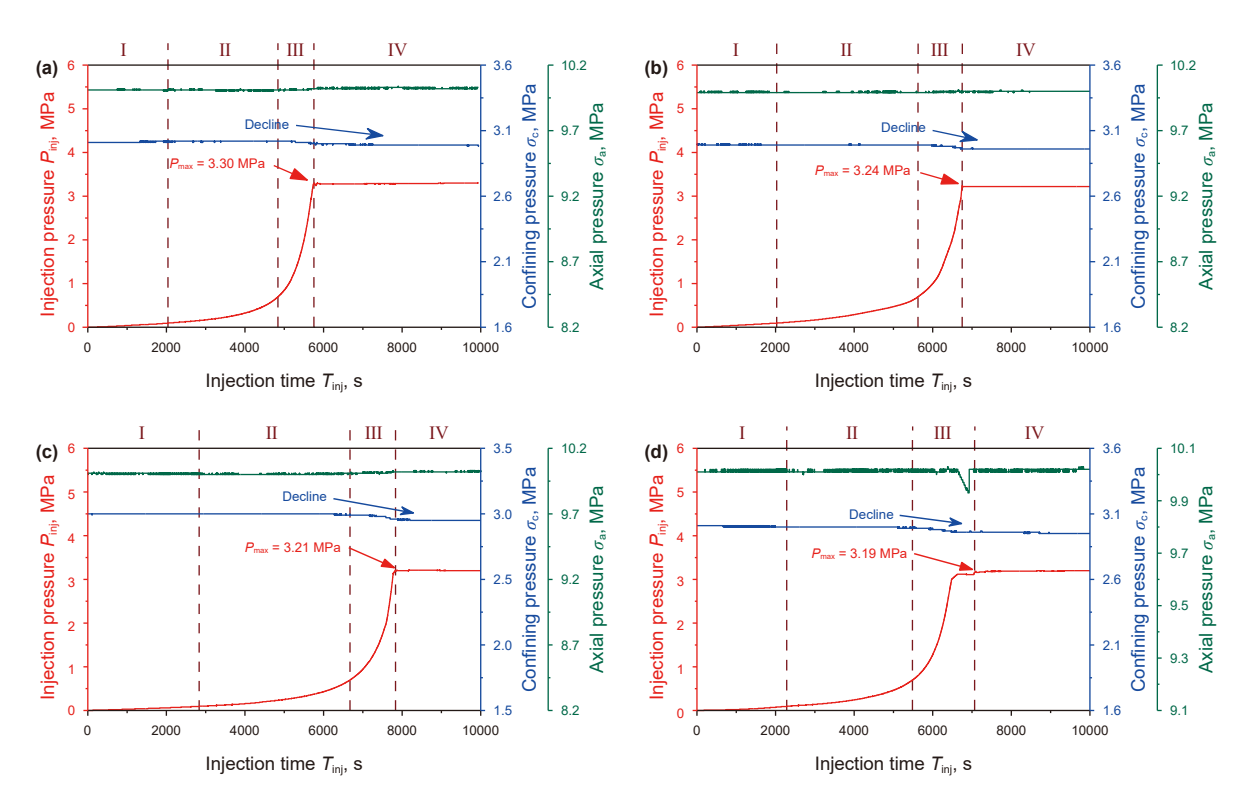


Fig. 4. Curves of injection pressure, axial pressure and confining pressure over time. (a) Specimen #1 ($\alpha = 0^{\circ}$), (b) specimen #2 ($\alpha = 15^{\circ}$), (c) specimen #3 ($\alpha = 30^{\circ}$), (d) specimen #4 ($\alpha = 45^{\circ}$).

a gradual increase during the slow pressurization stage, with the $P_{\rm ini}$ not rising significantly. Subsequently, the $P_{\rm ini}$ continued to increase steadily, before rapidly accelerating and eventually stabilizing at its maximum value. For example, when $\alpha=0^\circ$ (specimen #1), P_{inj} increased slowly during the slow pressurization stage (I), taking 2041 s to rise from 0 to 0.10 MPa. This slow pressure buildup corresponds to the initial water filling of the prefabricated fracture space. With water injected continuously, the increasing rate of P_{ini} accelerated significantly. It took 3199 s for $P_{\rm inj}$ to increase from 0.10 MPa to 0.70 MPa. A critical threshold was observed at $P_{\text{inj}} = 0.70 \text{ MPa}$, beyond which the P_{inj} exhibited rapid escalation to 3.30 MPa. Thereafter, Pini remained almost unchanged. The rate of water penetration inside the specimen is comparable to the rate of water injection. Consequently, the $P_{\rm ini}$ stabilizes at 3.30 MPa despite ongoing water injection. However, the maximum P_{ini} is different for different α .

Fig. 5(a) shows the peak values of the $P_{\rm inj}$ at different α . The peak value of $P_{\rm inj}$ decreases with increasing α . At α equal to 0°, the peak value of $P_{\rm inj}$ is 3.30 MPa. At 15°, the peak value of $P_{\rm inj}$ decreases to 3.24 MPa, which is a 1.85% decrease compared to the peak value at $\alpha=0^\circ$. As the α increases to 30°, the peak value of $P_{\rm inj}$ decreases to 3.21 MPa, which is 0.93% less than the peak value of $P_{\rm inj}$ at α of 15°. When the α is 45°, the peak value of $P_{\rm inj}$ is 3.19 MPa, which is a 0.62% decrease compared to the peak value at $\alpha=30^\circ$. Notably, specimen #4 ($\alpha=45^\circ$) exhibited characteristic axial pressure behavior, showing a distinct reduction after the rapid increase in $P_{\rm inj}$ before recovering to the preset 10 MPa (Fig. 4(d)). This phenomenon can be attributed to localized axial damage within the specimen, induced by the application of uniaxial compressive forces. The associated material properties and detailed characterization data are provided in the Appendix.

Furthermore, the experimental data reveal an inverse correlation between $P_{\rm inj}$ and $\sigma_{\rm c}$. Specifically, $\sigma_{\rm c}$ demonstrates a progressive decline in response to the rapid increase in $P_{\rm inj}$ (see Fig. 4). The variation of the confining pressure decrease ($\Delta\sigma_{\rm c}$) with α is statistically analyzed and presented in Fig. 5(b). It can be observed that $\Delta\sigma_{\rm c}$ increases with the increase of α . The minimum of $\Delta\sigma_{\rm c}$ is observed for specimen #1 ($\alpha=0^{\circ}$), which is 0.02 MPa. As α increases to 15°, $\Delta\sigma_{\rm c}$ increases to 0.03 MPa. At $\alpha=30^{\circ}$, $\Delta\sigma_{\rm c}$ increases to 0.06 MPa. As α further increases to 45°, $\Delta\sigma_{\rm c}$ reaches its maximum value of 0.07 MPa. At the rapid pressurization stage (III), some of the water breaks through the pore throat resistance and seeps to the surface of the specimen, subtly affecting $\sigma_{\rm c}$. The

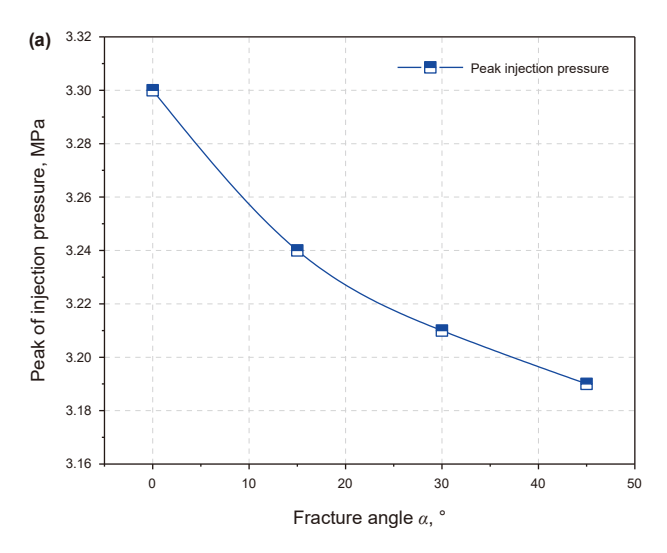
observed minimal fluctuations in $\Delta \sigma_{\rm C}$ (\leq 0.07 MPa) remain below the activation threshold of the confining pressure pump's compensation mechanism, resulting in a sustained deviation from the initial confining pressure following minor pressure decay.

3.2. Water infiltration and infiltration evolution

MRI images can visualize the migration and distribution of pore water during the injection process (Zhao et al., 2024b). In Fig. 6, black denotes the water-free zone, whereas the blue to red color gradient reflects increasing water content. This transition indicates a gradual increase in the infiltration of water. Due to limitations in device parameters, the evolution trend of the main infiltration zone is the only information that can be reliably obtained. The length of the infiltration zone along the radial direction of the specimen is defined as the width of the infiltration zone, and the length of the infiltration zone along the axial direction is defined as the length of the infiltration zone (see Fig. 6).

Fig. 6 shows the evolution of the water infiltration zone in different α specimens during the injection process. As shown in Fig. 6, during the slow pressurization stage (I), the water injected into the specimen primarily fills the prefabricated fracture space, with only a small portion of water penetrating into the rock pores ($P_{\rm inj}=0.10$ MPa). Water preferentially infiltrates both walls of the prefabricated fracture during water injection, regardless of the α . As α increases, the rate of water infiltration on the right wall of the prefabricated fracture continuously exceeds that on the left side. With $P_{\rm inj}$ increases, the infiltration zone gradually expands. The difference in the α leads to different infiltration zones.

For the same $P_{\rm inj}$, specimens with $\alpha=0^\circ$ exhibit the largest infiltration zone compared to other angles (15°, 30°, 45°). Upon the water's complete filling of the prefabricated fracture space and $P_{\rm inj}$ subsequent stabilized rise (stabilized pressurization stage (II)), water preferentially infiltrates more prominently from both sides of the prefabricated fracture. It extends throughout the specimen in the radial direction, near the specimen's surface ($P_{\rm inj}=0.70$ MPa). When $P_{\rm inj}$ reaches its peak (end of the rapid pressurization stage (III)), the infiltration zone extends to the specimen bottom. At $\alpha=15^\circ$, the infiltration zone width at a $P_{\rm inj}$ of 0.70 MPa is smaller than that at 0 MPa. In addition, that is different from the case when α is equal to 0°, as the infiltration zone does not spread to the bottom of the specimen when $P_{\rm inj}$ reaches its maximum value. The infiltration zone width at 0.70 MPa is



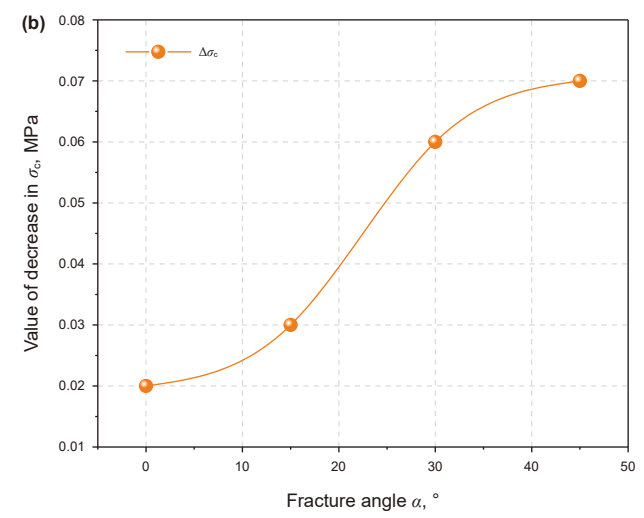


Fig. 5. Diagram of the influence of prefabricated fracture angle on the peak value of injection pressure and confining pressure. (a) Peak value of the injection pressure variation diagram with α . (b) Diagram of the value of the decrease in confining pressure with α .

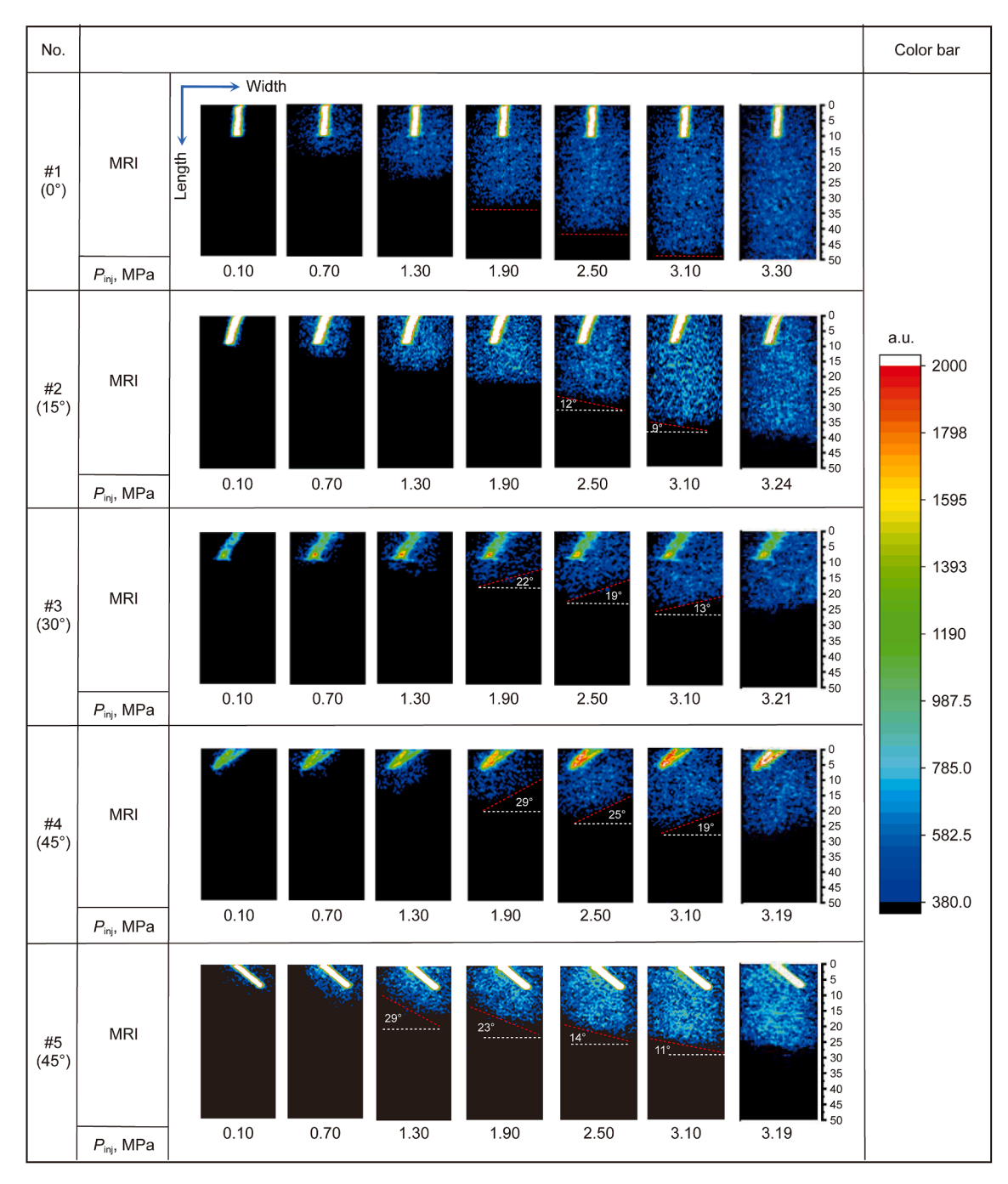


Fig. 6. Evolution diagram of infiltration zone during the water injection process.

shortened again when α increases to 30°. When the α is further escalated to 45°, there is a notable decrease in the infiltration zone's width, as compared to a 30° angle, under the $P_{\rm inj}$ pressures ranging from 0.10 MPa to 1.90 MPa.

The α significantly affects both the width and length of infiltration zones. To quantify the variation in the infiltration zone length during water injection at different α values, Fig. 7 presents the trend of changes in the infiltration zone length. Overall, at the same $P_{\rm inj}$, the infiltration zone length decreases as the α value increases; whereas, during the water injection process, the infiltration zone length expands as $P_{\rm inj}$ rises. Compared to the other α (15°, 30°, 45°), the infiltration zone length is maximum for the same $P_{\rm inj}$ at α equal to 0°. By the end of the water injection process,

the infiltration zone length has increased by 38.75 mm, from 11.25 mm to 50.00 mm. At $\alpha=15^\circ$, the infiltration zone length increases from 10 mm to 41.67 mm (a 31.67 mm increase) as $P_{\rm inj}$ rises from 0.10 MPa to 3.23 MPa. Compared to $\alpha=0^\circ$, the length of the maximum infiltration zone is reduced by 16.66%. When α reached 30°, compared with specimen #2 ($\alpha=15^\circ$), the increase in the infiltration zone length with $P_{\rm inj}$ slowed, growing from 9.17 mm to 26.67 mm, a total gain of 17.50 mm. For specimen #4 ($\alpha=45^\circ$), the variation in the infiltration zone length with $P_{\rm inj}$ is similar to that observed in specimen #3 ($\alpha=30^\circ$). Within the range of $P_{\rm inj}$ from 0.10 MPa to 1.90 MPa, the infiltration zone length in specimen #4 is notably shorter than that in specimen #3. However, once $P_{\rm inj}$ surpassed 1.90 MPa, the difference in the

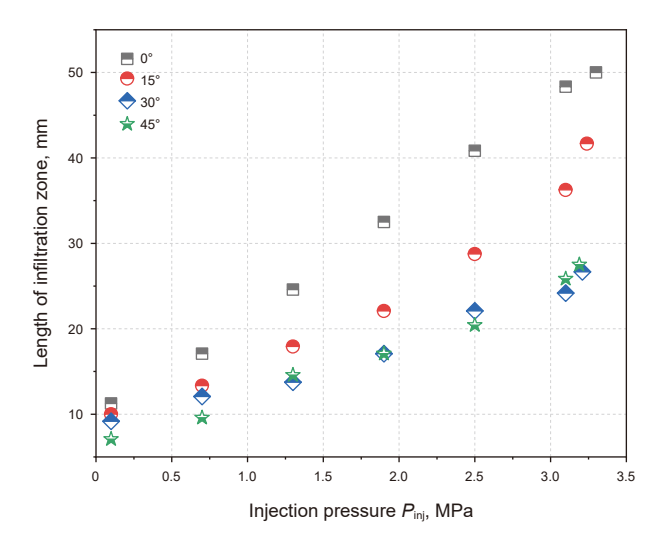


Fig. 7. Length evolution of the infiltration zone.

infiltration zone length between the two specimens became negligible, with a maximum difference of just 0.83 mm at the highest $P_{\rm inj}$.

The research has demonstrated that the wet-dry boundary formed by water infiltration is a pivotal factor influencing the initiation and propagation of hydraulic fractures (Li et al., 2023b). During water injection, the wet-dry boundary evolves as P_{ini} increases. For simplicity and clarity, the wet-dry boundary is called the water infiltration front. Different α have different effects on the evolution of the water infiltration front (see red dashed line in Fig. 6). When $\alpha = 0^{\circ}$, the water infiltration front becomes nearly horizontal after reaching the specimen edge through radial penetration. However, when α increases to 15°, 30°, and 45°, the water infiltration front becomes increasingly tilted, with its inclination angle growing proportionally with α . At α is equal to 15° and $P_{\rm ini}$ is increased to 2.50 MPa, the water infiltration front exhibits an inclination angle of 12°. Furthermore, the inclination angle of the water infiltration front demonstrates a gradual decrease with subsequent increases in P_{inj} . At the maximum recorded injection pressure of 3.24 MPa, the water infiltration front attains its minimum inclination angle of 8°. As α increases to 30°, the maximum inclination angle of the water infiltration front is 22°, which occurs at a $P_{\rm ini}$ of 1.90 MPa. Similar to specimen #3 ($\alpha = 15^{\circ}$), the inclination angle of the water infiltration front decreases as P_{inj} increases. As α is increased to 45°, the angle of inclination of the water infiltration front further increases. At a $P_{\rm inj}$ of 1.90 MPa, the water infiltration front attains its maximum inclination angle of 29°. Subsequently, the inclination angle decreases progressively from 25° to 15° as P_{inj} increases from 2.50 MPa to its peak value of 3.17 MPa. To further verify the influence of cleavage plane inclination on water infiltration front characteristics, we prepared a comparative specimen #5 with identical fracture geometry and experimental parameters to those of specimen #4. The primary distinction lies in the orientation of prefabricated fractures between specimens #4 and #5 during water injection, where specimen #5 exhibits an inverse prefabricated fracture orientation relative to specimen #4, as detailed in Table 1. During the water injection process, the water infiltration front demonstrates a consistent directional alignment with the prefabricated fracture, reaching a maximum inclination angle of 29° , equivalent to that observed in specimen #4. Similar to other specimens (specimens #1, #2, #3, and #4), the angle of inclination decreases as $P_{\rm ini}$ increases. The analysis reveals a positive correlation between the

parameter α and the inclination angle of the water infiltration front, demonstrating that the water infiltration front's angle increases progressively with higher values of α .

When $P_{\rm inj}$ rapidly rises and attains its maximum value, some of the water in the infiltration zone infiltrates radially towards the surface of the specimen. The water that breaks through the pore throat resistance and reaches the surface of the specimen exerts a slight impact on the $\sigma_{\rm c}$, causing a minor decrease in the $\sigma_{\rm c}$. Due to the reduction in the length of the infiltration zone as α increases (as illustrated in Fig. 7), the number of channels for water to infiltrate radially towards the specimen surface decreases. Consequently, fewer infiltration channels lead to a higher $P_{\rm inj}$ at the point of breakthrough compared to when there are more infiltration channels. The higher $P_{\rm inj}$ has a more significant impact on the $\sigma_{\rm c}$ and ultimately leads to an increase in the $\Delta\sigma_{\rm c}$ as α increases (see Fig. 5(b)).

MRI signals are generally visualized as gray images, and extracting the gray values of the gray images can quantify the content of hydrogen nuclei (1H) within the specimen and further characterize water infiltration. The MRI gray values in Fig. 6 are summarized in Fig. 8. Overall, at the same $P_{\rm inj}$, the cumulative gray value decreases as the angle α increases. Conversely, as P_{inj} rises, the cumulative gray value notably increases. At the same P_{ini} , the maximum cumulative gray value is observed when the angle α is 0°, suggesting that a natural fracture oriented at 0° near the well is more conducive to water infiltration under the same injection conditions. When α equals 0°, as $P_{\rm inj}$ increases from 0.10 MPa to the maximum value of 3.30 MPa, the cumulative gray value shows the largest increase, increasing by a factor of 12.82. With α increasing to 15 $^{\circ}$, the cumulative gray values decrease gradually across all $P_{\rm ini}$. Specifically, compared to α equals 0° , when $P_{\rm inj}$ is 0.10 MPa, the cumulative gray value experiences a reduction of 38.77%. Similarly, when $P_{\rm ini}$ increases to its maximum value of 3.24 MPa, the cumulative gray value decreases by 39.78%. Namely, the increase in α reduces water infiltration. As α increases to 30°, the cumulative gray value significantly decreases. At the $P_{\rm ini}$ of 0.10 MPa, the cumulative grayscale values account for 15.54% and 16.17% at α of 0° and 15° , respectively. When $P_{\rm ini}$ reaches its maximum value (3.21 MPa), the increment in cumulative gray value becomes relatively small, being only 38.02% and 39.59% of the cumulative gray values observed at $\alpha = 0^{\circ}$ and $\alpha = 15^{\circ}$, respectively. When α is further increased to 45°, it is found that the cumulative gray values for each stage do not differ significantly from those of specimen #3, where α is equal to 30°. In conclusion, under the same $P_{\rm ini}$

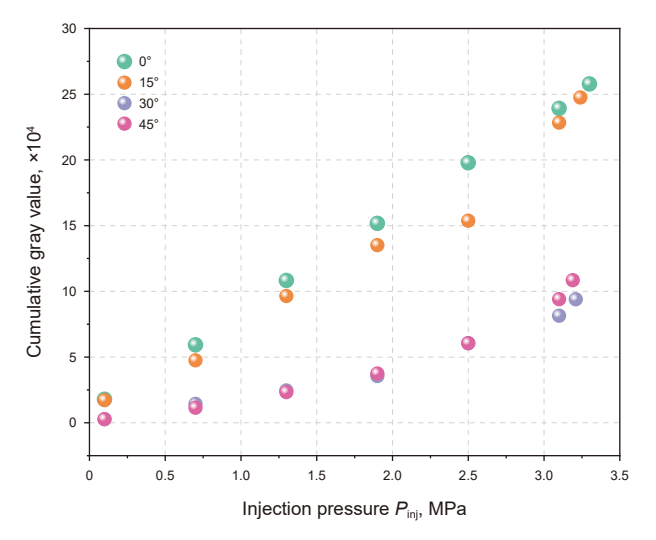


Fig. 8. Evolution of cumulative gray values.

condition, the smaller the angle α is, the more favorable the conditions for water infiltration become.

To gain a deeper understanding of the impact of water pressurization on the water infiltration rate at each stage, we calculated the rate of increase in the cumulative gray value at each stage of the water injection process, as illustrated in Fig. 9. It can be seen that the rate of increase in the cumulative gray value decreases with increasing P_{ini} , irrespective of the α . Prior to the onset of the rapid pressurization stage (III) when $P_{\rm inj}$ is below 0.70 MPa, the cumulative gray value exhibits its maximum rate of increase. During the initial water injection phase, the cumulative growth rate of the gray value exceeds 1.50 for various values of α . It indicates that despite the relatively low P_{inj} , the slow water pressurization rate, and the limited infiltration area, water infiltration occurs at the fastest rate. As P_{inj} rapidly increases, the growth rate of the cumulative gray value decreases sharply. When $P_{\rm ini}$ exceeds 1.30 MPa, the growth rate of the cumulative gray value drops below 0.50, indicating a significant slowdown in the water infiltration rate during the rapid pressurization stage (III). Besides, at the maximum P_{inj} , the differences in cumulative gray value growth rates between $\alpha = 0^{\circ}$ and $\alpha = 15^{\circ}$, and between $\alpha = 30^{\circ}$ and $\alpha = 45^{\circ}$, are insignificant. Specifically, the cumulative gray value growth rates at the maximum $P_{\rm ini}$ are 0.077 for $\alpha=0^{\circ}$, 0.083 for $\alpha=15^{\circ}$, 0.154 for $\alpha = 30^{\circ}$, and 0.153 for $\alpha = 45^{\circ}$, respectively. In summary, during the process of water injection, water infiltration occurs more rapidly during the slow pressurization stage (I) and stabilized pressurization stage (II). However, the water infiltration rate gradually slows down after the P_{inj} rapidly increases.

3.3. Distribution characteristics of pore structure

Fig. 10 shows the evolution of T_2 during water injection for different α . Water distributed in pores of different apertures has different transverse relaxation times in the magnetic field (Wang et al., 2022b). Changes in the T_2 curve can reflect the evolution of the pores of the specimen. In general, regardless of how the α changes, the increase in $P_{\rm inj}$ during water injection primarily affects the adsorption pores (T_2 at 0.01–10 ms) and some seepage pores (T_2 at 10–100 ms), while the larger seepage pores (T_2 > 100 ms) undergo relatively little change. Within the 0.50–100 ms range, the rightward shift of the T_2 curve with increasing $P_{\rm inj}$ indicates a progressive expansion of pore space volume in the corresponding pore system during water injection.

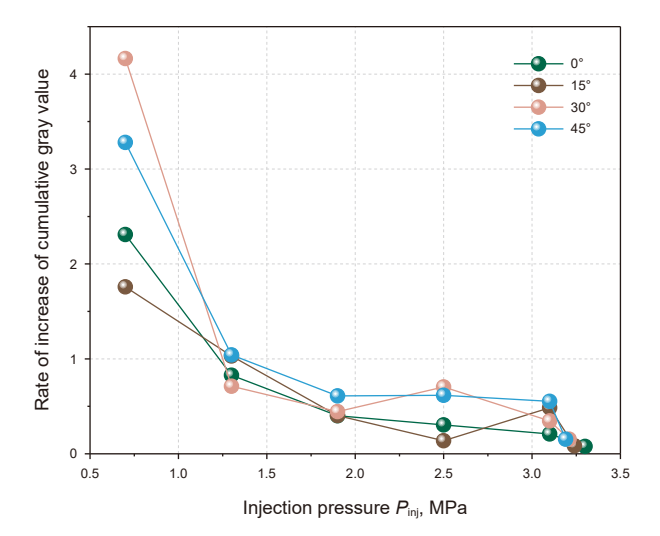


Fig. 9. Evolution of cumulative gray value growth rate with injection pressure.

For different α , subtle variations in pore behavior trends are observed with respect to P_{ini} variations, particularly when relaxation times are below 0.55 ms. We zoom in on the portion of the curve with relaxation time ranging from 0.05 ms to 0.58 ms to analyze the migration mechanism of fluid in this part of the pore during pressurization. For the sake of brevity, we refer to this part of the micropore as a nanopore to describe the changes occurring in this section of the pore during water injection. It should be noted that the definition of nanopore used in this study is intended solely for brevity and clarity. Consequently, it is possible that the nanopore relaxation time ranges identified in this study do not align with those established by other authors. For specimen #1 $(\alpha=0^{\circ})$, when $P_{\rm inj}$ is increased from 0.10 MPa to 1.30 MPa, the T_2 curve shifts left within the 0.01-0.55 ms range and simultaneously shifts upward in amplitude. This change in the T_2 curve suggests that during the slow pressurization stage (I), stabilized pressurization stage (II), and initial periods of the rapid pressurization stage (III), more water migrates into the nanopores. With a further increase in P_{inj} (in rapid pressurization stage (III)), the curve shifts rightward and downward in the range of 0.02-0.43 ms, indicating that the nanopores decreased. When α is 15°, 30°, and 45°, generally, the change in nanopores follows a trend of increasing first and then decreasing with an increase in P_{inj} , analogous to the behavior observed in specimen #1 ($\alpha = 0^{\circ}$). However, slight differences in the variation of T_2 exist due to different α .

Observation of the T_2 local magnification plots for different specimens reveals that the magnitude of the rightward shift of the T_2 curve decreases with an increase in α (see Fig. 10). At $\alpha = 0^{\circ}$, the T_2 curve shifts rightward and downward within the relaxation time range of 0.02-0.43 ms as P_{inj} increases. This range progressively narrows to 0.02–0.29 ms and 0.02–0.22 ms as α increases to 15° and 30°, respectively. Notably, when α reaches 45°, the shift range of the T_2 curve converges with that observed in specimen #3. It indicates that the ability to change the pore size of the nanopores during water injection gradually decreases with an increase in α . In addition, the magnitude of the shift of T_2 curves to the right and downward decreases with the increase of α . It is observed that the magnitude is largest at α equal to 0°, followed by 15°, and smallest at 30° and 45°. In conclusion, although the trends of the T_2 curves in the adsorption pore range are similar during an increase in P_{inj} , the difference in α leads to different changes in some of the nanopore structures after P_{inj} reaches its maximum value.

The distribution of the corresponding pore space can be obtained by integrating the T_2 curve over the relaxation time. To gain a deeper understanding of how the cleavage angle α impacts the pore structure of the specimen during water injection, a statistical analysis of pore distribution is conducted for various α values, as shown in Fig. 11. It is worth noting that before $P_{\rm inj}$ reaches 0.10 MPa (slow pressurization stage (I)), the injected water primarily fills the prefabricated fracture space, with relatively little water penetrating into the pores of the specimen. Overall, as Pinj increases, the percentage of water infiltration into adsorption pores decreases, while the percentage of water infiltration into seepage pores increases. When α is 0° , as $P_{\rm inj}$ increases from 0.70 MPa to its maximum value of 3.30 MPa (in rapid pressurization stage (III)), the proportion of adsorption pores decreases from 54.33% to 39.20%, representing a decrease of 15.13%. The percentage of seepage pores increases from 45.67% to 60.80%. When α is 15°, the percentage of adsorption pores decreases from 52.79% to 43.30%, a reduction of 9.49%, as $P_{\rm inj}$ increases from 0.70 MPa to its maximum value of 3.21 MPa. As α is increased to 30°, it is observed that the percentage of adsorption pores decreases from 62.89% to 38.79%, whereas the percentage of seepage pores increases from 37.11% to 61.21%. When α increases to 45° with $P_{\rm inj}$ rising from 0.70 MPa to

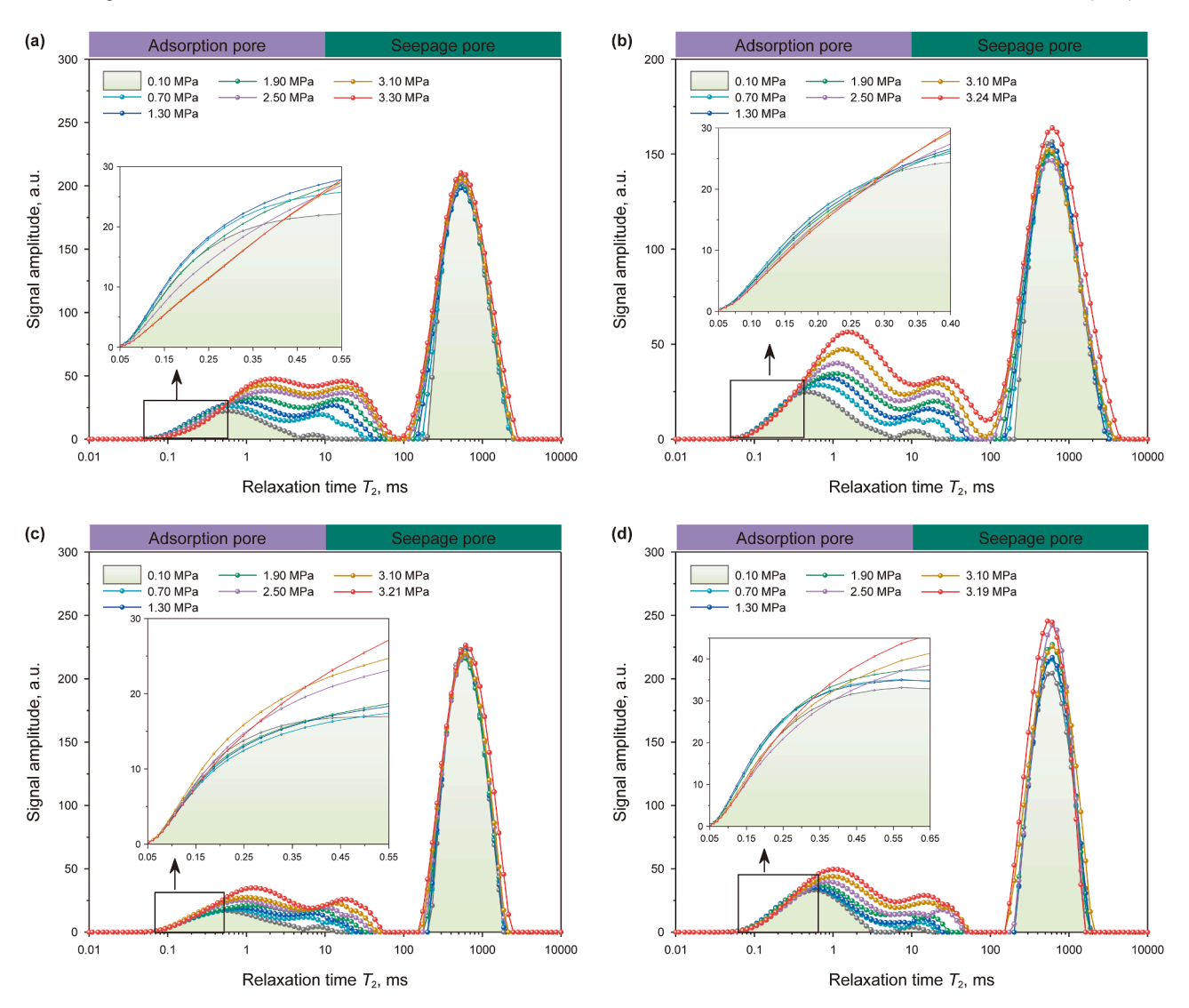


Fig. 10. T_2 curve evolution of the injection process. (a) Specimen #1 ($\alpha = 0^{\circ}$), (b) specimen #2 ($\alpha = 15^{\circ}$), (c) specimen #3 ($\alpha = 30^{\circ}$), (d) specimen #4 ($\alpha = 45^{\circ}$).

its maximum value of 3.19 MPa, the adsorption pore proportion decreases by 13.20%. In summary, as $P_{\rm inj}$ increases, the proportion of water infiltration within the adsorption pores decreases. During the rapid pressurization stage (III), the conversion of adsorption pores into seepage pores is accelerated.

4. Discussion

4.1. Mechanisms of water infiltration and pore damage

Fig. 12 shows a schematic diagram of water infiltration and migration during the water injection process. Once water enters and permeates into the specimen, the pores within the infiltration zone of the specimen remain partially filled with water. As shown in Fig. 12(a), in the slow pressurization stage (I), the amplitude of T_2 is relatively low due to limited water infiltration during the low injection pressure ($P_{\rm inj} < 0.10$ MPa). As the $P_{\rm inj}$ increases, a greater amount of water infiltrates into the specimen, filling an increasing number of adsorption and seepage pores (see Fig. 12(b)). Furthermore, during the slow pressurization stage (I) and stabilized pressurization stage (II), the infiltration volume is minimal, causing some of the micropores within the specimen to remain partially unfilled by the infiltrated water, thereby forming

unsaturated pores (see Fig. 12(c)). As the P_{inj} increases, more water infiltrates into the specimen, triggering progressive infiltration zone expansion. The micropores that are initially partially filled reach complete water saturation, and additional micropores are also filled (see Fig. 12(b)-(d)). On the one hand, when water penetrates the sandstone, some minerals (montmorillonite and illite) dissolve, which in turn increases the internal pore aperture of the specimen (Shi et al., 2024). On the other hand, with a subsequent increase in P_{inj} , these saturated pores are affected by pore pressure. The rock matrix moves outward under the action of pore stress, resulting in a slight increase in pore size (see Fig. 12(d)-(e)). In addition, during the rapid pressurization stage (III), the P_{ini} increases rapidly, promoting water infiltration while helping to convert adsorption pores into seepage pores. Therefore, as the $P_{\rm ini}$ increases, the proportion of adsorption pores in the specimen gradually decreases, while the proportion of seepage pores gradually increases.

Changes in the T_2 curve reflect the variations of moisture content within the specimen. The increasing T_2 amplitude with rising $P_{\rm inj}$ indicates a corresponding growth in the moisture content of the sandstone during fluid pressurization (Fig. 10). Notably, the T_2 curve first migrates leftward and upward, then displaces rightward and downward (0.01–0.55 ms, see Fig. 10), revealing

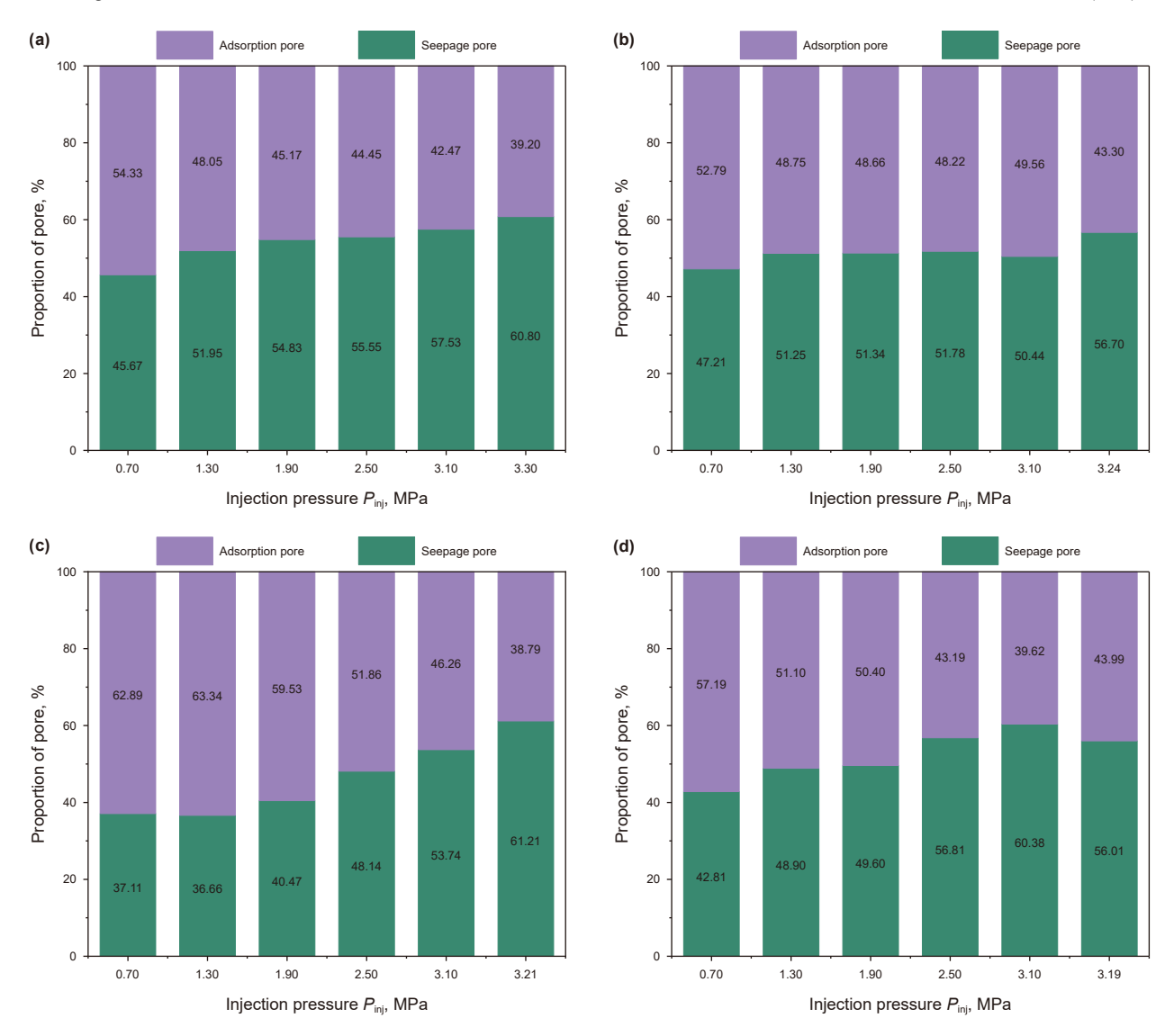


Fig. 11. Pore evolution during the water injection process. (a) Specimen #1 ($\alpha = 0^{\circ}$), (b) specimen #2 ($\alpha = 15^{\circ}$), (c) specimen #3 ($\alpha = 30^{\circ}$), (d) specimen #4 ($\alpha = 45^{\circ}$).

sequential pore space saturation and subsequent pressure-induced pore dilation during water injection (Zhao et al., 2019a). In this study, since the $P_{\rm inj}$ is kept below 3.30 MPa (see Fig. 4), the resulting pore pressure in the infiltration zone is too low to create new pores in the specimen. Thus, the increasing pore size (rightward and downward shift in T_2 curve with increasing $P_{\rm inj}$) can be primarily attributed to the expansion of pores due to the increase in pore pressure.

Moreover, previous studies have demonstrated that water infiltration creates a pressure gradient within the infiltration zone of sandstone, with the pore pressure gradually decreasing from the infiltration point toward the periphery of the infiltration zone (Zhou et al., 2020). Consequently, the pore damage caused by water injection is predominantly focused near the prefabricated fracture (see Fig. 6). The study conducted by Stanchits et al. (2011) further supports our conclusions. As the $P_{\rm inj}$ rises, the infiltration zone progressively expands, leading to an increase in the distance between the prefabricated fracture (infiltration point) and the outer edge of the infiltration zone. As the distance increases, the pore pressures in proximity to the water infiltration front become nearly uniform, resulting in comparable diffusion rates within the infiltration zone. Hence, for a given α , the inclination of the water

infiltration front decreases as the $P_{\rm inj}$ increases (see Fig. 6). This variation suggests that the primary direction of the fluid infiltration and migration is closely dependent on the injection pressure and the spatial distribution of pore pressure within the sandstone. Specifically, the higher injection pressures and the larger infiltration zone promote a more uniform pressure distribution, which in turn influences the fluid infiltration pathways and the overall migration behavior.

4.2. Influence of prefabricated fracture angle on water infiltration

Sandstone is a sedimentary rock composed of cemented sand grains, characterized by tiny pores between the sand grains that function as channels for fluid infiltration (Zou et al., 2012). When a fluid comes into contact with the sandstone under fluid pressure, it infiltrates (or penetrates) along the pores into the sandstone (Shi et al., 2024; Wang and Zhou, 2024). For reservoirs containing fractures, after the interior of the fracture is filled with fluid, the fluid pressure acts directly on the walls and tip of the fracture. In this study, it has been observed that before water infiltration along the radial direction of the specimen reaches its surface, the infiltration on the prefabricated fracture's walls is considerably greater

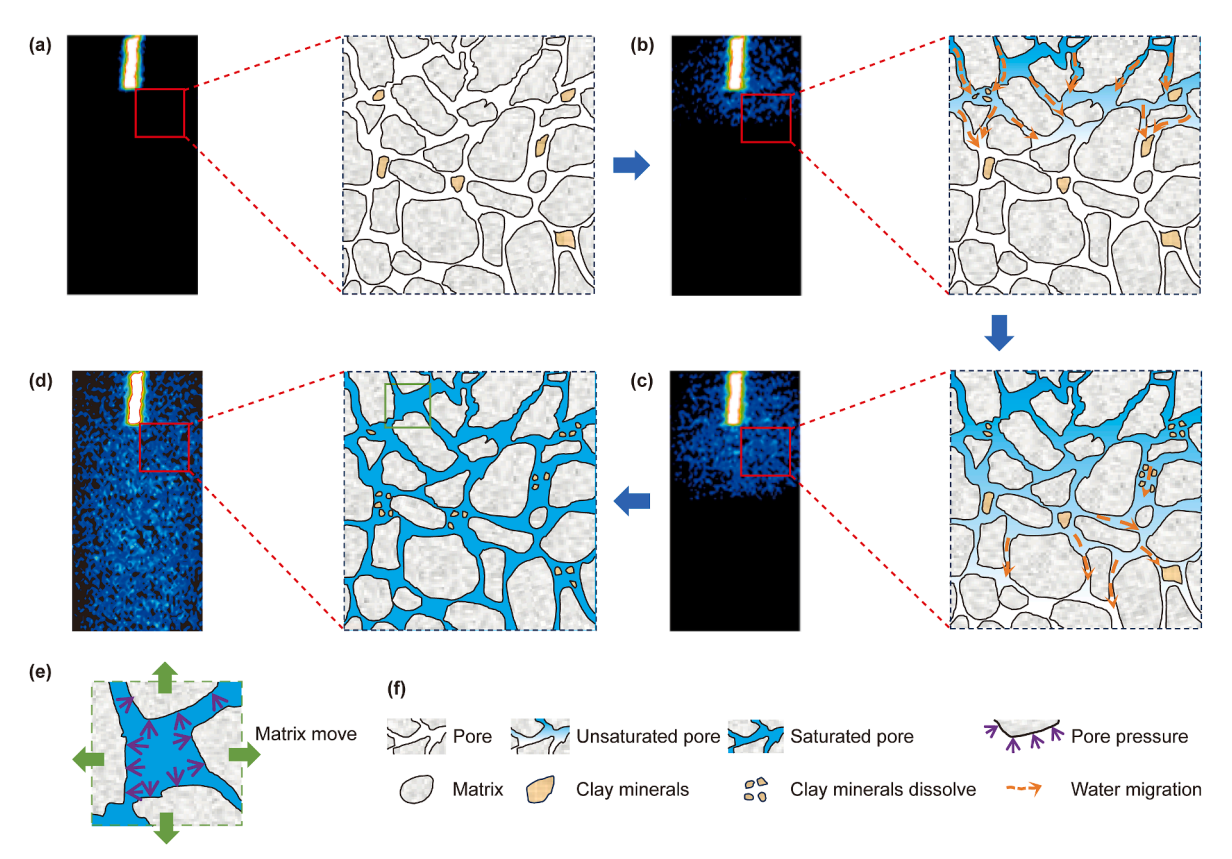


Fig. 12. Schematic diagram of the dynamic migration mechanism of water. (a) Stage (I): pore distribution, (b) stage (II): water infiltration, (c) stage (III): unsaturated infiltration zone, (d) stage (IV): saturated infiltration zone, (e) increased pore size, (f) legend.

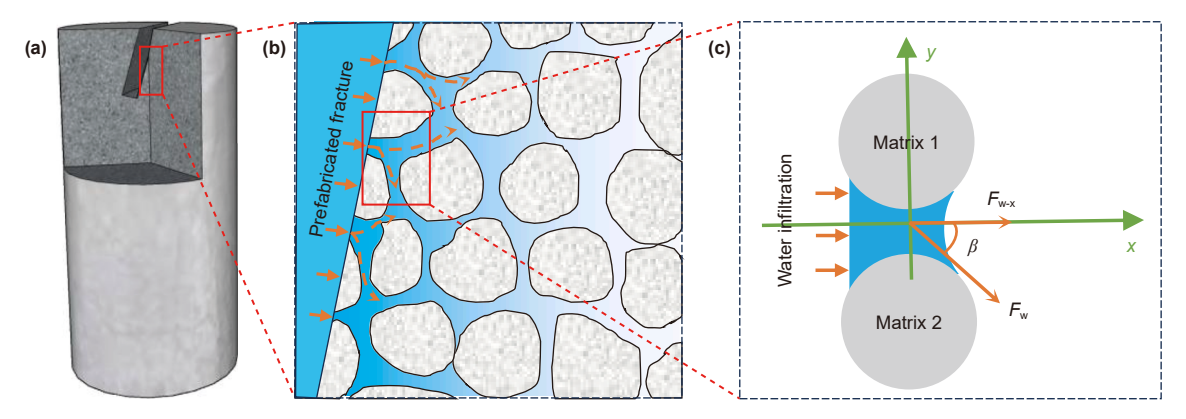


Fig. 13. Schematic diagram of water infiltration mechanism. (a) Sandstone specimen, (b) water migration, (c) water pressure.

than at the prefabricated fracture's tip. This observation is similar to the phenomenon reported by Li et al. (2023b) and Shen et al. (2024). The area of the prefabricated fracture walls is significantly larger than the cross-sectional area at the tip of the prefabricated fracture where it contacts the water. As the contact area increases, so does the number of water infiltration channels, making it easier for water to infiltrate. Thus, during water injection, the water preferentially permeates along the prefabricated fracture wall faster than at the prefabricated fracture tip, resulting in an infiltration zone whose width is greater than its height. However, in this study, the advantage of water infiltration along the prefabricated fracture wall diminishes once the water penetrates the specimen surface, due to the specimen's size limitation.

With the increase in α , the width of the radial infiltration zone of water decreases at the same $P_{\rm inj}$ (see Fig. 6). Since the direction of water force is perpendicular to the plane in which the force is applied, changes in α result in corresponding changes in the direction of the water force within the specimen. The water force that accumulates within prefabricated fractures with different α values exerts different forces on their walls. In this study, to facilitate the description of the change of fluid force direction, the angle between the direction of the water force $(F_{\rm W})$ acting on the wall of the prefabricated fracture and the radial direction of the specimen is defined as β . We have produced a sandstone pore map depicting the impact of water infiltration on the pore, as shown in Fig. 13. As can be seen from Fig. 13(b) when α is 0° , β equals 0° , the direction of the water force acting on the prefabricated fracture

wall is consistent with the *x*-direction, and $F_{\text{W-}x} = F_{\text{W}}$. With the increase in α , β increases gradually, and $F_{\text{W-}x} = \cos\beta \cdot F_{\text{W}}$. Consequently, $F_{\text{W-}x}$ gradually decreases as α increases. Under the same P_{inj} , the width of the infiltration zone decreases as α increases.

Similar to the observations of Wang et al. (2024), the infiltration zone expands gradually with increasing fluid pressure. In addition, the geometry of internal fractures in the rock heavily influences fluid invasion geometries (Babadagli et al., 2015; Hatami and Walsh, 2022). In this study, we observe that variations in prefabricated fracture angle (α) significantly affect both the size and morphology of the infiltration zone. As can be seen in Fig. 6, α affects the length of the infiltration zone and the angle of the water infiltration front. During water injection, water infiltrates from the walls and tips of the prefabricated fracture. Since there are far more infiltration channels on both walls of the prefabricated fracture than at the tip, the water mainly flows or penetrates along both walls. At α equals 0° , the infiltration area on both walls of the prefabricated fracture remains uniform, resulting in an approximately equal rate of water infiltration from both walls. Consequently, the water infiltration front appears nearly horizontal. With the increase in α , the difference in the area of direct contact with water on both walls of the prefabricated fracture becomes progressively more significant. Due to the cylindrical geometry of the specimens employed in this study, the effective area of the prefabricated fracture wall opposing the inclination angle decreases progressively with increasing α , consequently leading to a reduction in the corresponding infiltration channels. As a result. the rate of water infiltration from the wall of the prefabricated fracture opposite the inclination decreases, leading to a change in the shape of the infiltration zone. Moreover, the water infiltration front demonstrates a distinct inclination. Furthermore, as α increases, the difference in water infiltration rate between the two walls of the prefabricated fracture widens, causing the water infiltration front angle to increase correspondingly and resulting in the water infiltration front inclination angle increasing with α (see

4.3. Implications for field fracturing

Understanding the mechanisms of water interaction with reservoir rocks at each stage of injection is crucial for field fracturing design. For tight sandstone reservoirs, pore damage induced by water injection is particularly critical for the formation of hydraulic fractures and the enhancement of reservoir permeability. Based on the experimental findings, we recommend optimizing field fracturing operations through injection parameter adjustments, particularly by increasing injection rates, to minimize the duration of the initial slow pressurization stage (I) and enhance overall fracturing efficiency. The duration of the rapid pressurization stage (III) in the fracturing process can be effectively extended through two primary approaches: reducing the injection rate or implementing a constant pressure injection strategy. These approaches promote enhanced water infiltration throughout the reservoir matrix, accelerate the transformation of adsorption pores into seepage pores across extended regions, intensify nearwellbore formation damage, establish optimal conditions for hydraulic fracture initiation, and ultimately improve overall reservoir permeability.

In addition, research has shown that compared to natural fractures with large fracture angles, the smaller the angle of natural fractures near the wellbore, the more favorable it is for fluid infiltration, forming a larger infiltration zone and facilitating the evolution from adsorption pores to seepage pores. Therefore, during field fracturing, it is recommended to investigate the degree and distribution of natural fractures in the reservoir. When

the fracturing section is set in a reservoir with natural fractures, adjust the orientation of the perforation so that the angle between the injection direction and the fractures is as small as possible, with 0° being the optimal angle.

However, it should be noted that during the rapid pressurization phase, fluid pressure can cause damage to pores, accompanied by fluid infiltration, making it difficult to accurately quantify the relationship between the increase in fluid pressure and pore damage. We will explore this research field through numerical simulations in future studies.

5. Conclusions

This study systematically investigated the influence of nearwellbore fracture angle (α) on water infiltration, migration patterns and pore evolution mechanisms through RT-NMR technology. The evolution of T_2 and MRI were monitored in real-time during water injection. The variations in $P_{\rm inj}$ across different prefabricated fracture inclinations were systematically analyzed, while the characteristics of pore evolution and water migration were investigated through the comprehensive analysis of T_2 and MRI. Finally, the mechanism underlying the influence of α on water infiltration and pore evolution during water injection was discussed, and practical insights for field fracturing operations were derived based on the experimental findings. The main conclusions are as follows:

- (1) Water infiltration exhibits distinct characteristics under different injection pressures. During the slow pressurization stage (I), water primarily flows into the prefabricated fractures. With water injected continuously, the stabilized pressurization stage (II) exhibits maximum infiltration rates despite the low P_{inj} and the limited infiltration zone. The majority of pore damage occurs during the rapid pressurization stage (III), where higher pressures drive significant structural changes within the specimen.
- (2) Water infiltration facilitates the transformation of pores from unsaturated to saturated conditions. Elevating the injection pressure expands pores in the saturated zone and transforms adsorption pores into seepage pores, with adsorption pores progressively diminishing. Due to the pressure gradient in the infiltration zone, injection-induced damage is predominantly focused in the vicinity of the nearwellbore fracture.
- (3) The prefabricated fracture angle (α) significantly influences water infiltration and migration. The fastest rate and largest infiltration zone occur at $\alpha=0^{\circ}$, while the smallest appears at $\alpha=45^{\circ}$. Infiltration rates are consistently higher along the fracture walls than at the tip, regardless of α , and the infiltration front inclination increases with α .
- (4) The experimental findings suggest optimizing fracturing parameters by aligning the perforation direction (injection direction) parallel to the fracture orientation, reducing the slow pressurization duration, and extending the rapid pressurization stage.

CRediT authorship contribution statement

Sheng-Feng Wu: Writing – original draft, Investigation. Yong-Fa Zhang: Writing – review & editing, Methodology, Investigation. Yu Zhao: Resources, Project administration, Methodology, Funding acquisition. Chao-Lin Wang: Writing – review & editing. Jing Bi: Writing – review & editing. An-Fa Long: Data curation. Yan Li: Data curation.

Declaration of competing interest

The authors declare that they have no known competing financial interests or personal relationships that could have appeared to influence the work reported in this paper.

Acknowledgment

This research was supported by National Natural Science Foundation of China (Nos. 52364004, 52464005), The Youth Talent Growth Project of Guizhou Provincial Department of Education (No. QianJiaoJi[2024]18), Postgraduate Research Fund of Guizhou Province in 2024 (No. 2024YJSKYJJ067), Basic Research Project of Guizhou University (No. [2023]40), Guizhou Provincial Basic Research Program (Natural Science) (No. QianKeHeJiChu-ZK[2024] YiBan011), and Research Fund for Talents of Guizhou University (No. GuiDaRenJiHeZi(2023)24).

Appendix A. Supplementary data

Supplementary data to this article can be found online at https://doi.org/10.1016/j.petsci.2025.06.018.

References

- Abe, A., Kim, T.W., Horne, R.N., 2021. Laboratory hydraulic stimulation experiments to investigate the interaction between newly formed and preexisting fractures. Int. J. Rock Mech. Min. Sci. 141, 104665. https://doi.org/10.1016/j.ijrmms.2021.104665.
- Babadagli, T.F., Ren, X.J., Develi, K., 2015. Effects of fractal surface roughness and lithology on single and multiphase flow in a single fracture: an experimental investigation. Int. J. Multiphas. Flow 68, 40–58. https://doi.org/10.1016/j.ijmultiphaseflow.2014.10.004.
- Bandara, K.M.A.S., Ranjith, P.G., Kumari, W.G.P., 2022. A coupled X-ray imaging and experimental permeability study of propped hydraulically induced fractures. Rock Mech. Rock Eng. 55 (5), 2581–2596. https://doi.org/10.1007/s00603-021-02566-0
- Chang, X., Xu, E., Guo, Y.T., Yang, C.H., Hu, Z.W., Guo, W.H., 2022. Experimental study of hydraulic fracture initiation and propagation in deep shale with different injection methods. J. Pet. Sci. Eng. 216, 110834. https://doi.org/10.1016/j.petrol.2022.110834.
- Chitrala, Y., Moreno, C., Sondergeld, C., Rai, C., 2013. An experimental investigation into hydraulic fracture propagation under different applied stresses in tight sands using acoustic emissions. J. Pet. Sci. Eng. 108, 151–161. https://doi.org/10.1016/j.petrol.2013.01.002.
- Fazio, M., Chandler, M.R., Sauter, M., 2023. Permeability evolution of bentheim sandstone at simulated georeservoir conditions. Sci. Rep. 13 (1), 16171. https://doi.org/10.1038/s41598-023-42826-3.
- Fazio, M., Ibemesi, P., Benson, P., Bedoya-González, D., Sauter, M., 2021. The role of rock matrix permeability in controlling hydraulic fracturing in sandstones. Rock Mech. Rock Eng. 54 (10), 5269–5294. https://doi.org/10.1007/s00603-021-02580-2.
- Fu, H.F., Huang, L.K., Hou, B., Weng, D.W., Guan, B.S., Zhong, T.X., Zhao, Y.L., 2024. Experimental and numerical investigation on interaction mechanism between hydraulic fracture and natural fracture. Rock Mech. Rock Eng. 57 (12), 10571–10582. https://doi.org/10.1007/s00603-024-04101-3.
- Ge, X.M., Zhao, J.E., Zhang, F.S., Fan, Y.R., Liu, J.Y., Cai, J.C., Nie, S.D., Wang, C.J., 2019. A practical method to compensate for the effect of echo spacing on the shale NMR T₂ spectrum. Earth Sp. Sciences (1969) 6 (8), 1489–1497. https://doi.org/10.1029/2018FA000540
- Geng, W.L., Wang, J.D., Zhang, X.C., Huang, G., Li, L., Guo, S.L., 2023. Experimental study of pore structure and rock mechanical properties of tight sandstone after acid treatment. Acta Geotech 18 (12), 6559–6571. https://doi.org/10.1007/ s11440-023-02094-x.
- Hatami, S., Walsh, S.D.C., 2022. Relative permeability of two-phase flow through rough-walled fractures: effect of fracture morphology and flow dynamics. J. Hydrol. 613, 128326. https://doi.org/10.1016/j.jhydrol.2022.128326.
- Jia, A.L., Wei, Y.S., Guo, Z., Wang, G.T., Meng, D.T., Huang, S.Q., 2022. Development status and prospect of tight sandstone gas in China. Nat. Gas. Ind. B. 9 (5), 467–476. https://doi.org/10.1016/j.ngib.2022.10.001.
- Jia, W.H., Zhou, H.W., Xie, S.L., Wang, Y.M., Hu, X.F., Zhang, L., 2024. Pore-pressure and stress-coupled creep behavior in deep coal: insights from real-time NMR analysis. Int. J. Min. Sci. Technol. 34 (1), 77–90. https://doi.org/10.1016/j. iimst.2023.12.001.
- Jia, Y.Z., Song, C.P., Wang, J.H., Gan, Q., 2021. The breakdown process of lowpermeable shale and high-permeable sandstone rocks due to non-aqueous

- Jiang, C.B., Niu, B.W., Yin, G.Z., Zhang, D.M., Yu, T., Wang, P., 2019. CT-based 3D reconstruction of the geometry and propagation of hydraulic fracturing in shale. J. Pet. Sci. Eng. 179, 899–911. https://doi.org/10.1016/j.petrol. 2019.04.103.
- Lamont, N., Jessen, F.W., 1963. The effects of existing fractures in rocks on the extension of hydraulic fractures. J. Petrol. Technol. 15 (2), 203–209. https://doi.org/10.2118/419-pa.
- Li, C.Z., Liu, G.D., Cao, Z., Yuan, W., Wang, P., You, Y., 2020. Analysis of petrophysical characteristics and water movability of tight sandstone using low-field nuclear magnetic resonance. Nat. Resour. Res. 29 (4), 2547–2573. https://doi.org/ 10.1007/s11053-019-09582-6.
- Li, S.H., Zhang, S.C., Ma, X.F., Zou, Y.S., Li, N., Chen, M., Cao, T., Bo, Z.K., 2019. Hydraulic fractures induced by water-/carbon dioxide-based fluids in tight sandstones. Rock Mech. Rock Eng. 52 (9), 3323–3340. https://doi.org/10.1007/s00603-019-01777-w.
- Li, X.Y., Lei, X.L., Shen, H.M., Li, Q., 2023a. Fracturing around dry/wet boundary in tight sandstones monitored by micro-seismicity in laboratory. Rock Mech. Rock Eng. 56 (5), 3693–3708. https://doi.org/10.1007/s00603-023-03241-2.
- Li, X.Y., Lei, X.L., Li, Q., 2023b. Laboratory hydraulic fracturing in layered tight sandstones using acoustic emission monitoring. Geoenergy Sci. Eng. 223, 211510. https://doi.org/10.1016/j.geoen.2023.211510.
- Liu, P., Ju, Y., Gao, F., Ranjith, P.G., Zhang, Q.B., 2018. CT identification and fractal characterization of 3-D propagation and distribution of hydrofracturing cracks in low-permeability heterogeneous rocks. J. Geophys. Res. Solid Earth 123 (3), 2156–2173. https://doi.org/10.1002/2017JB015048.
- Liu, Y.L., Zheng, X.B., Peng, X.F., Zhang, Y.Y., Chen, H.D., He, J.H., 2022. Influence of natural fractures on propagation of hydraulic fractures in tight reservoirs during hydraulic fracturing. Mar. Petrol. Geol. 138, 105505. https://doi.org/ 10.1016/j.marpetgeo.2021.105505.
- Liu, Z.Y., Chen, M., Zhang, G.Q., 2014. Analysis of the influence of a natural fracture network on hydraulic fracture propagation in carbonate formations. Rock Mech. Rock Eng. 47 (2), 575–587. https://doi.org/10.1007/s00603-013-0414-7.
- Lu, Y.Y., Wang, L., Ge, Z.L., Zhou, Z., Deng, K., Zuo, S.J., 2020. Fracture and pore structure dynamic evolution of coals during hydraulic fracturing. Fuel 259, 116272. https://doi.org/10.1016/j.fuel.2019.116272.
- Ma, D.D., Cheng, C.K., Ding, C.D., Song, J.L., Hu, D.W., 2021. Comparisons of fracturing mechanism of tight sandstone using liquid CO₂ and water. J. Nat. Gas Sci. Eng. 94, 104108. https://doi.org/10.1016/j.jngse.2021.104108.
- Shen, H.M., Yoon, J.S., Zang, A., Hofmann, H., Li, X.Y., Li, Q., 2024. Impact of injection pressure and polyaxial stress on hydraulic fracture propagation and permeability evolution in graywacke: insights from discrete element models of a laboratory test. J. Rock Mech. Geotech. Eng. 17 (4), 2344–2359. https://doi.org/10.1016/j.jrmge.2024.05.017.
- Shi, F.K., Sun, X.M., He, L.S., Ding, J.X., Tao, Z.G., Cui, L., 2024. Study on the mechanical characteristics and microscopic response mechanisms of sandstone under pressurized water absorption. Rock Mech. Rock Eng. 57 (5), 3197–3218. https://doi.org/10.1007/s00603-024-03759-z.
- Stanchits, S., Mayr, S., Shapiro, S., Dresen, G., 2011. Fracturing of porous rock induced by fluid injection. Tectonophysics 503 (1–2), 129–145. https://doi.org/10.1016/j.tecto.2010.09.022.
- Stanchits, S., Surdi, A., Gathogo, P., Edelman, E., Suarez-Rivera, R., 2014. Onset of hydraulic fracture initiation monitored by acoustic emission and volumetric deformation measurements. Rock Mech. Rock Eng. 47 (5), 1521–1532. https:// doi.org/10.1007/s00603-014-0584-y.
- Wang, K., Zhang, X., Guo, H.J., Fu, Q., Wang, D.K., Zhang, H., Lu, F.C., 2022a. Experimental study on hydraulic fracturing of laminated sandstone combined with industrial CT and L-NMR. Geofluids 2022, 5716346. https://doi.org/ 10.1155/2022/5716346.
- Wang, C.L., Zhao, Y., Ning, L., Bi, J., 2022b. Permeability evolution of coal subjected to triaxial compression based on in-situ nuclear magnetic resonance. Int. J. Rock Mech. Min. Sci. 159, 105213. https://doi.org/10.1016/j.ijrmms. 2022 105213
- Wang, H.J., Li, J., Guo, Q., Shi, R.G., Zhao, Z.J., Zhang, Y.T., Zhao, F., 2021. Experimental study on the influence of water on the failure properties of sandstone. Bull. Eng. Geol. Environ. 80 (10), 7747–7771. https://doi.org/10.1007/s10064-021-02410-3.
- Wang, H.Y., Zhou, D.S., Zou, Y., Zheng, P., 2024. Effect mechanism of seepage force on the hydraulic fracture propagation. Int. J. Coal Sci. Technol. 11 (1), 223–240. https://doi.org/10.1007/s40789-024-00695-9.
- Wang, H.Y., Zhou, D.S., 2024. Mechanistic study on the effect of seepage force on hydraulic fracture initiation. Fatig. Fract. Eng. Mater. Struct. 47 (5), 1602–1619. https://doi.org/10.1111/ffe.14269.
- Wei, D., Gao, Z.Q., Fan, T.L., Wang, S.S., Li, C.C., Li, H., 2017. Experimental hydraulic fracture propagation on naturally tight intra-platform shoal carbonate. J. Pet. Sci. Eng. 157, 980–989. https://doi.org/10.1016/j.petrol.2017.08.016.
- Xu, W.J., Zhao, J.Z., Rahman, S.S., Li, Y.M., Yuan, Y.D., 2019. A comprehensive model of a hydraulic fracture interacting with a natural fracture: analytical and numerical solution. Rock Mech. Rock Eng. 52 (4), 1095–1113. https://doi.org/ 10.1007/s00603-018-1608-9.
- Yan, H., Zhang, J.X., Li, B.Y., Zhu, C.L., 2021. Crack propagation patterns and factors controlling complex crack network formation in coal bodies during tri-axial supercritical carbon dioxide fracturing. Fuel 286, 119381. https://doi.org/ 10.1016/j.fuel.2020.119381.

- Zeng, L.B., Liu, H.T., 2010. Influence of fractures on the development of low-permeability sandstone reservoirs: a case study from the Taizhao district, Daqing Oilfield, China. J. Pet. Sci. Eng. 72 (1–2), 120–127. https://doi.org/10.1016/j.petrol.2010.03.009.
- Zhang, Y.F., Long, A.F., Zhao, Y., Zang, A., Wang, C.L., 2023. Mutual impact of true triaxial stress, borehole orientation and bedding inclination on laboratory hydraulic fracturing of Lushan shale. J. Rock Mech. Geotech. Eng. 15 (12), 3131–3147. https://doi.org/10.1016/j.jrmge.2023.02.015.
- Zhang, Y.F., Zhao, Y., Zang, A., Long, A.F., 2024. Acoustic emission evolution and hydraulic fracture morphology of Changning shale stressed to failure at different injection rates in the laboratory. Rock Mech. Rock Eng. 57 (2), 1287–1308. https://doi.org/10.1007/s00603-023-03586-8.
- Zhang, Y.F., Long, A.F., Zang, A., Zhao, Y., 2025. Pore-scale damage evolution in sandstone induced by fluid infiltration under various stress conditions. Int. J. Rock Mech. Min. Sci. 193, 106181. https://doi.org/10.1016/j.ijrmms.2025.106181.
- Zhang, Z.Y., Weller, A., 2014. Fractal dimension of pore-space geometry of an Eocene sandstone formation. Geophysics 79 (6), D377–D387. https://doi.org/10.1190/GEO2014-0143.1.
- Zhao, J.Z., Wang, Q., Hu, Y.G., Zhao, C.N., Zhao, J., 2019a. Prediction of pore pressure-induced stress changes during hydraulic fracturing of heterogeneous reservoirs through coupled fluid flow/geomechanics. J. Eng. Mech. 145 (12), 05019001. https://doi.org/10.1061/(asce)em.1943-7889.0001672.
- Zhao, Y., Wu, S.F., Zhang, Y.F., Long, A.F., Huang, H.S., Li, Y., 2024a. Effect of wellbore orientation and axial stress on hydraulic fracture initiation and propagation in

- Lushan shale with inclined bedding planes. Rock Mech. Rock Eng. 57 (12), 10551–10570. https://doi.org/10.1007/s00603-024-04107-x.
- Zhao, Y., Yang, Z.Y., Wang, C.L., Bi, J., 2024b. Experimental investigation on the effects of microwave irradiation in pore structures of LN₂ freezing coal for coalbed methane extraction. Rock Mech. Rock Eng. 57 (9), 7495–7513. https://doi.org/10.1007/s00603-024-03883-w.
- Zhao, Y., Zhang, Y.F., He, P.F., 2019b. A composite criterion to predict subsequent intersection behavior between a hydraulic fracture and a natural fracture. Eng. Fract. Mech. 209, 61–78. https://doi.org/10.1016/j.engfracmech.2019.01.015.
- Zhou, D.S., Wang, H.Y., He, Z.X., Liu, Y.F., Liu, S., Ma, X.L., Cai, W.B., Bao, J.Q., 2020. Numerical study of the influence of seepage force on the stress field around a vertical wellbore. Eng. Appl. Comput. Fluid Mech. 14 (1), 1489–1500. https://doi.org/10.1080/19942060.2020.1835733.
- Zhou, D.W., Zhang, G.Q., Zhao, P.Y., Wang, Y.Y., Xu, S.F., 2018. Effects of post-instability induced by supercritical CO₂ phase change on fracture dynamic propagation. J. Pet. Sci. Eng. 162, 358–366. https://doi.org/10.1016/j.petrol. 2017.12.066.
- Zhuang, L., Kim, K.Y., Jung, S.G., Diaz, M., Min, K.B., 2019. Effect of water infiltration, injection rate and anisotropy on hydraulic fracturing behavior of granite. Rock Mech. Rock Eng. 52 (2), 575–589. https://doi.org/10.1007/s00603-018-1431-3.
- Zou, C.N., Zhu, R.K., Liu, K.Y., Su, L., Bai, B., Zhang, X.X., Yuan, X.J., Wang, J.H., 2012. Tight gas sandstone reservoirs in China: characteristics and recognition criteria. J. Pet. Sci. Eng. 88 (89), 82–91. https://doi.org/10.1016/j.petrol.2012.02.001.